

## Article

# Photothermal Effect and Phase Transition in VO<sub>2</sub> Enhanced by Plasmonic Particles

Vladimir Kaydashev <sup>1,\*</sup>, Boris Khlebtsov <sup>2,\*</sup> , Maxim Kutepov <sup>1</sup>, Anatoliy Nikolskiy <sup>3</sup>, Alexey Kozakov <sup>3</sup> , Alexey Konstantinov <sup>4</sup>, Alexey Mikheykin <sup>4</sup>, Gevork Karapetyan <sup>1</sup> and Evgeni Kaidashev <sup>1</sup> 

<sup>1</sup> Laboratory of Nanomaterials, Southern Federal University, 200/1 Stachki Ave., 344090 Rostov-on-Don, Russia

<sup>2</sup> Institute of Biochemistry and Physiology of Plants and Microorganisms RAS, Saratov Scientific Center, 13 Entuziastov Ave., 410049 Saratov, Russia

<sup>3</sup> Institute of Physics, Southern Federal University, 194 Stachki Ave., 344090 Rostov-on-Don, Russia

<sup>4</sup> Physics Faculty, Southern Federal University, 5 Zorge St., 344090 Rostov-on-Don, Russia

\* Correspondence: kaydashev@gmail.com (V.K.); khlebtsov\_b@ibppm.ru (B.K.)

**Abstract:** Phase change metasurfaces based on VO<sub>2</sub>, which are pre-heated with electric current and optically addressed by projected structured light hologram, are considered to become a new paradigm in programmed THz/middle IR flat optics. Macroscopic quasi-homogeneous arrays of Au nanoparticles show large near IR absorption and a significant photothermal effect capable of boosting a light-triggered switching of VO<sub>2</sub> and are to be carefully examined. We propose a new approach to simultaneously probe the altered temperature and electric conductivity of a hybrid Au particle-VO<sub>2</sub> film composite by monitoring a phase shift and attenuating a surface acoustic wave in a YX128° cut LiNbO<sub>3</sub> substrate. The method shows a temperature resolution of 0.1 °C comparable with the best existing techniques for studying nanoobjects and surfaces. The laser-induced photothermal effects were characterized in a macroscopic array of Au nanostars (AuNSts) with different surface coverage. In a monolayer of 10 nm Au, coupled plasmonic nanoparticles were deposited on the LiNbO<sub>3</sub> substrate. An optically triggered insulator-metal transition assisted by photothermal effect in AuNSts/VO<sub>2</sub>/TiO<sub>2</sub>/LiNbO<sub>3</sub> composites was studied at varied light power. We believe that the proposed SAW-based method is of significant importance for the characterization and optimization of radiation absorbing or/and electrically heated elements of metasurfaces and other devices for lab-on-chip and optical communication/processor technology.

**Keywords:** vanadium dioxide; VO<sub>2</sub>; photothermal effect; surface acoustic waves; SAW; nanostars; coupled plasmonic nanoparticles



**Citation:** Kaydashev, V.; Khlebtsov, B.; Kutepov, M.; Nikolskiy, A.; Kozakov, A.; Konstantinov, A.; Mikheykin, A.; Karapetyan, G.; Kaidashev, E. Photothermal Effect and Phase Transition in VO<sub>2</sub> Enhanced by Plasmonic Particles.

*Materials* **2023**, *16*, 2579. <https://doi.org/10.3390/ma16072579>

Academic Editor: Federico Cesano

Received: 15 February 2023

Revised: 13 March 2023

Accepted: 21 March 2023

Published: 24 March 2023



**Copyright:** © 2023 by the authors. Licensee MDPI, Basel, Switzerland. This article is an open access article distributed under the terms and conditions of the Creative Commons Attribution (CC BY) license (<https://creativecommons.org/licenses/by/4.0/>).

## 1. Introduction

Vanadium dioxide is considered one of the most promising materials with isolator-metal transition (MIT) to alter the phase and amplitude of passing or reflected middle IR, THz/GHz, and near IR waves [1,2]. VO<sub>2</sub> metasurfaces are considered effective tools to in-situ manipulate a radiation wavefront by thermal, electrical or optical signals to focus radiation [3], obtain beam steering [4], alter polarization [3,5], filter wavelength [6] or achieve ultrafast modulation [7] in a tunable manner. Also, VO<sub>2</sub> metasurfaces are prospective for developing lab-on-chip technology, optical chip-based self-trained neural networks and optical processing technologies. Recent advances in metasurfaces for manipulation of THz wavefront as well as the progress in VO<sub>2</sub>-based devices, are summarized in reviews [2,8,9].

We recently demonstrated a hybrid optoelectric approach for controlling VO<sub>2</sub>-based THz metasurface by pre-heating its pixels with electric current and switching them with laser light intensity as low as 0.3 W/cm<sup>2</sup> in near IR or UV range [10]. The approach allows one to address individual pixels with light holograms generated by a digital micromirror device (DMD). We believe that metasurfaces with pixels that are optically addressed by

projected structured light holograms will soon become a new paradigm in mid-IR/THz flat optics and photonics.

Plasmonic particles and nanosystems are well established as efficient light-to-heat nano-converters [11–14]. They are widely used in advanced healthcare for the selective killing of harmful cells in tissues and blood [15], as well as in highly efficient light absorbers [16] and thermophotovoltaics [17].

Recently we showed that plasmonic particles deposited on the surface of VO<sub>2</sub> might boost the performance of light-triggered MIT [10]. Namely, a laser-induced switching threshold was reduced by ~30% when the VO<sub>2</sub> metasurface was covered with a monolayer of Au particles. However, the switching efficiency of VO<sub>2</sub>, which is activated by a plasmonic particle, depends not only on the absorption of the plasmonic system but also on many features of a VO<sub>2</sub> film, including the MIT hysteresis loop steepness, possible defect-related metastable states and others, which are defined by preparation protocol of VO<sub>2</sub> and by crystalline properties of a substrate. Meanwhile, accurate control of minor temperature alterations due to the photothermal effect in hybrid Au-VO<sub>2</sub> metasurfaces with complicated topology is still challenging. Note that comprehensive control of a device's temperature and conductivity of its elements and an accurately chosen applied light intensity within addressing hologram are the key parameters to obtain advanced optical addressing of a metasurface. Once these issues are resolved, the design of a gradient metasurface with pixels switched to more than two states will become doable. As a result, the quality of several important applications, including focusing, polarization rotation, modulation and beam steering, would be improved. Indeed, the exact control of the temperature immediately on the surface, which can be different from the one at the back side of the sample or the heater surface, is a key important issue. Thus, in the case of optically triggered metasurfaces, the temperature data feedback should be obligatory in-situ, taken into account to optimally apply the needed laser light power to completely or partially switch the metasurface elements.

There are several methods to monitor the temperature of nanoparticle arrays or even individual nanoobjects [18–23]. Each method has some benefits and drawbacks in compatibility towards the object to characterize, achievable temperature resolution, range of working temperature, laboriousness, reliability, cost-efficiency, etc. These conditions may seriously limit the applicability of a particular method to study some specific type of object. For example, using thermocouples or IR thermometry, one typically may obtain averaged and not accurate results if special efforts were not undertaken. Among the more reliable optical methods, one should name luminescence nanothermometry [18], exploiting emission from quantum dots or a ruby substrate with incorporated Cr<sup>3+</sup> ions [19], Raman thermometry [20], as well as more delicate techniques such as holographic interferometry [21,22] or photothermal imaging [23].

We propose a new method that exploits surface acoustic waves (SAW) to simultaneously accurately monitor the altered temperature and electric conductivity of a hybrid Au particle-VO<sub>2</sub> composite film heated and exposed by laser light. The studied Au particle/VO<sub>2</sub>/TiO<sub>2</sub> multi-layer structures are deposited on the YX128° cut LiNbO<sub>3</sub> piezoelectric crystal where a SAW at 120 MHz may propagate—the surface heating results in the SAW velocity alteration, which is observed as the S<sub>21</sub> phase shift. The SAW phase shift is calibrated as a function of the bare LiNbO<sub>3</sub> substrate temperature and is further used to monitor crystal surface temperature variation induced by any process. In particular, we monitor laser-assisted heating induced by plasmonic particles. Additionally, the temperature-triggered alteration of sheet conductivity in VO<sub>2</sub> film due to MIT is in situ controlled by monitoring a SAW attenuation change.

In this study, we quantitatively characterize the photothermal effect in the macroscopic array of Au nanostars at varied surface coverage and in the monolayer of Au coupled particles deposited on VO<sub>2</sub>/TiO<sub>2</sub>/LiNbO<sub>3</sub> multi-layer structure as well as on the bare LiNbO<sub>3</sub> substrate. Furthermore, an optically triggered insulator-metal transition assisted by the photothermal effect was studied at varied light power. On a broader scale, the

proposed SAW-based method is expected to become a new cost-effective tool to accurately monitor surface temperature and sheet conductivity of phase change metasurfaces. It is more important for testing and optimizing their elements during design. Also, we believe that the method will be useful in studies of the various heat, electric or/and mechanical stress-related phenomena in nanosystems for nanoelectronics, photonics, metamaterials, plasmonics, terranostics and other fields.

## 2. Materials and Methods

### 2.1. Pulsed Laser Deposition of VO<sub>2</sub>/TiO<sub>2</sub> on Piezoelectric LiNbO<sub>3</sub> Substrates

VO<sub>2</sub>/TiO<sub>2</sub> films of 10 × 10 mm in Samples C, D and E were deposited on the central part of 10 × 20 mm YX-128° cut LiNbO<sub>3</sub> substrates using a pulsed laser deposition method. Radiation of KrF laser (at 248 nm, 10 Hz) was focused to a 2 × 5 mm square spot on a rotating VO<sub>2</sub> or TiO<sub>2</sub> targets to give a laser fluence of 2 J/cm<sup>2</sup>. The target to substrate distance was set to be 5 cm. First, a ~70 nm TiO<sub>2</sub> buffer layer was deposited on LiNbO<sub>3</sub> substrate at 640 °C in oxygen ambient at 3 × 10<sup>-2</sup> mbar for 2000 laser shots. Next, a ~130 nm VO<sub>2</sub> film was deposited at 560 °C an oxygen pressure of 2 × 10<sup>-2</sup> mbar.

### 2.2. Raman Spectroscopy and XPS Study of VO<sub>2</sub> Film

Raman spectra of VO<sub>2</sub>/TiO<sub>2</sub> films (Sample D) were studied using Renishaw inVia Reflex Raman spectrometer with a spectral resolution better than 1 cm<sup>-1</sup>. The samples were excited by the light of the Ar<sup>+</sup> laser at 514 nm with a power density less than using ×50 long focal distance objective (NA = 0.5). Raman scattering was collected in the backward direction. Crossed polarizers were not used. The incident laser power was minimized to avoid local sample heating.

X-ray photoelectron spectroscopy (XPS) experiments were carried out using Thermo Scientific ESCALAB 250 system with a monochromatic Al-Kα X-ray source. The energy resolution is 0.6 eV, as found from the observation of the Ag 3d<sub>5/2</sub> line. The sample was exposed with an X-ray beam 500 microns in diameter. The binding energies were obtained using a calibration line of C 1 s at 285.0 eV.

### 2.3. Fabrication of Quasi-Homogeneous Monolayers of Au Nanostars

First, 15 nm spherical Au seeds were prepared by adding 3.1 mL 1% sodium citrate to 100 mL of boiling 0.01% chloroauric acid on a magnetic stirrer (700 rpm). Within 15 min, the color of the solution changed from colorless to orange–red. The final Au concentration was 1.6 × 10<sup>12</sup> mL<sup>-1</sup>. Next, 1 mL of polyvinylpyrrolidone (10 kDa, 100 mg/mL in ethanol) was added to 100 mL of Au nanoparticles under stirring (700 rpm). The mixture was allowed to react for 1 h. The PVP-coated Au seeds were centrifuged twice (12,000 rpm, 45 min), the supernatant was discarded, and the particles were dispersed in 4 mL of ethanol to achieve a final Au concentration of 4 × 10<sup>13</sup> mL<sup>-1</sup>. Next, AuNSt were prepared following a modification of the standard PVP/DMF approach [24]. First, 10 g of PVP was dissolved in 100 mL of DMF. Next, an aqueous solution of 0.2 mL 120 mM HAuCl<sub>4</sub> was added, followed by 0.2 mL of seeds. Within 150 min, the color of the solutions changed from colorless to deep blue, indicating the formation of AuNSt. Finally, the AuNSt were cleaned via centrifugation (7500 rpm, 20 min) and resuspended in 20 mL of H<sub>2</sub>O. The final concentration of nanostars was 4 × 10<sup>11</sup> mL<sup>-1</sup>, corresponding to optical density 8 at the plasmon resonance wavelength (as measured in the cuvette of 1 cm length).

A representative TEM image of as-prepared nanostars is shown in Figure 1b. The particles have an average size of about 70 nm and consist of a 30–40 nm core accompanied by 5–10 tips. This particle structure results in the main plasmon peak at a wavelength of 820 nm, as shown in Figure 1a.

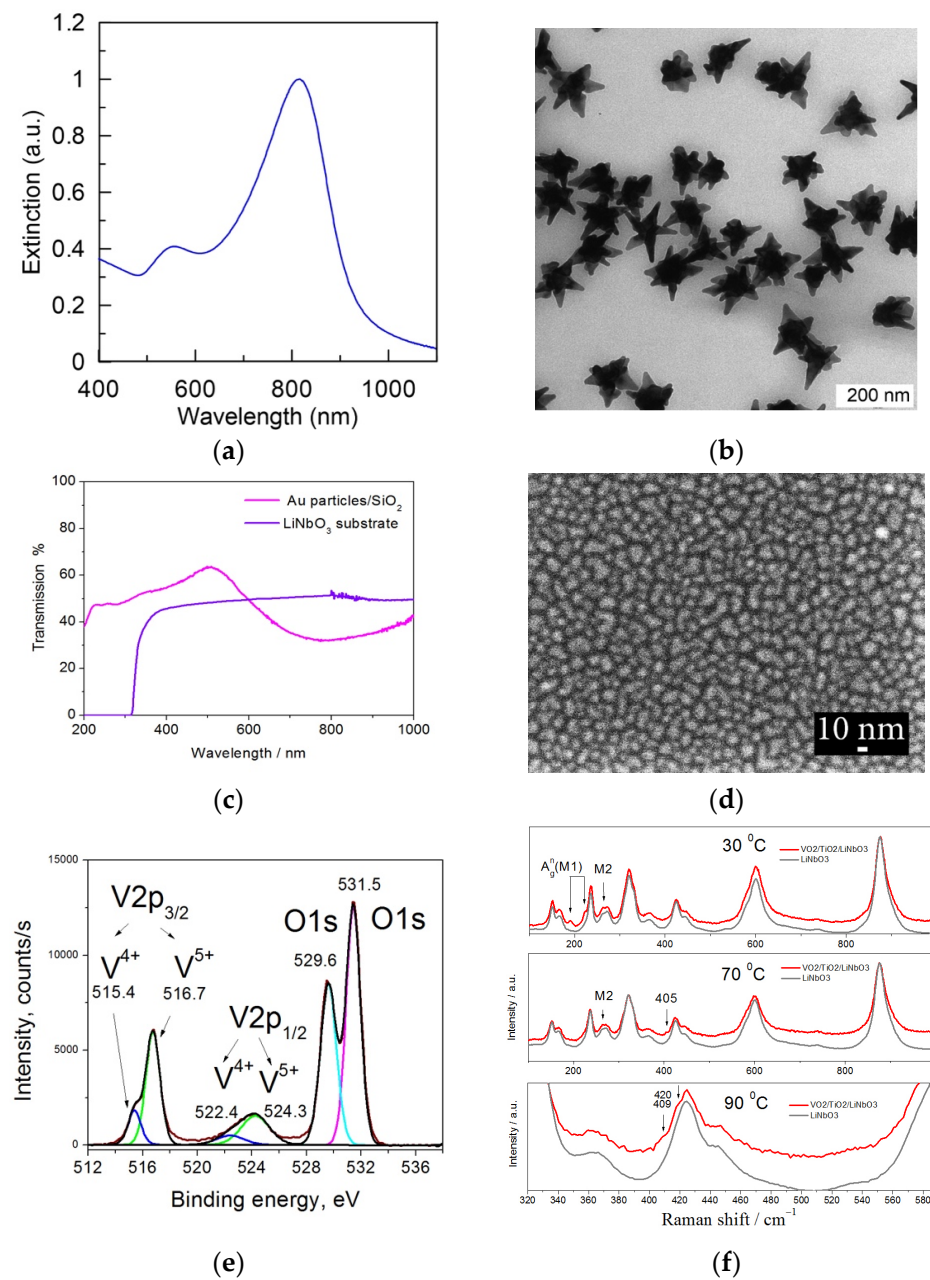


**Figure 1.** (a) Normalized extinction spectra of AuNSts used in Samples A, C–E; (b) representative TEM image of the nanostars; (c) optical transmission spectrum of Au coupled plasmonic particles similar to those deposited in sample Sample B and transmission of bare YX-128°-cut LiNbO<sub>3</sub> double-side polished substrate; (d) SEM image of Au coupled plasmonic particles in Sample B; (e) XPS spectra of VO<sub>2</sub> films on the TiO<sub>2</sub>/LiNbO<sub>3</sub> substrate. The fitting of the spectrum with multiple peak functions is shown by colored curves; (f) Raman spectra of Sample D at different temperature taken in the area of VO<sub>2</sub>/TiO<sub>2</sub> film and of a bare LiNbO<sub>3</sub> substrate.

The LiNbO<sub>3</sub> substrates were cleaned with ethanol and immersed into 0.1% polyvinylpyridine (PVPir, 160 kDa, 0.1% ethanol solution) for 3 h. Then, samples were washed with ethanol and water. VO<sub>2</sub>/TiO<sub>2</sub>/LiNbO<sub>3</sub> substrates were then placed into nanostars solutions with particle concentrations of 4, 1 and 0.5 × 10<sup>11</sup> mL<sup>-1</sup> to obtain Sample C–E correspondingly. Bare LiNbO<sub>3</sub> substrate and the nanostars solutions with particle concentration of 2 × 10<sup>11</sup> mL<sup>-1</sup> were used to get Sample A. The samples were incubated for 4 h to promote nanoparticle adsorption. After incubation, substrates were washed with water, dried and stored at ambient conditions until use.

#### 2.4. PLD of a Monolayer of Au Plasmonic Coupled Nanoparticles

A quasi-homogeneous self-assembled macroscopic monolayer of 5–10 nm Au coupled plasmonic nanoparticles (Sample B) shown in Figure 1d was prepared using the PLD method in Ar ambient at 0.7 m bar for 400 laser shots.

Due to some distribution of size, ellipticity and inter-particle separating gaps in the array of coupled nanoparticles, the observed absorption band is significantly broadened as it is a superposition of many plasmonic bands of individual particles. For ~10 nm particles, the scattering absorption is predominant, and the input of light scattering is minor. As a result, the transmission spectrum reveals a characteristic broad band near ~780 nm and a shoulder in the blue/UV range of ~250–450 nm, as shown in Figure 1c.

#### 2.5. Characterization and Measurements

We use the setup shown in Figure 2a to in-situ monitor the samples' surface temperature and conductivity change. Surface acoustic wave (SAW) is excited in the samples deposited on the LiNbO<sub>3</sub> substrate. Two YX-128° cut LiNbO<sub>3</sub> substrates with a one-directional inter-digital transducer (IDT) on each piece were used to generate and detect a SAW. We use the standard LiNbO<sub>3</sub> YX128° cut, a reasonably widely available LiNbO<sub>3</sub> crystal cut on the market, which gives the optimal effective electromechanical coupling coefficient and, thus, allows one to obtain the lowest SAW propagation losses without additional efforts. Furthermore, IDTs are designed to have a central frequency of 120 MHz and an aperture of 1.2 mm. Thus, the generated SAW propagates in the acoustic channel of the same width. Therefore the channel width where SAW is propagating is also only 1.2 mm or a bit smaller.

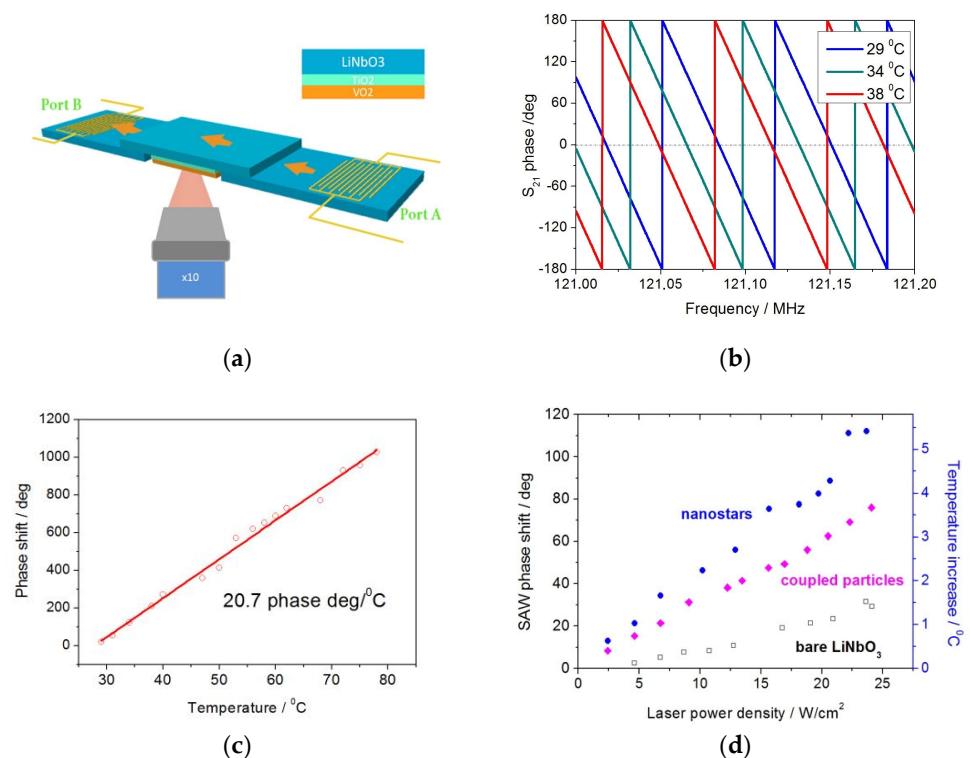


**Figure 2.** Sketch of the experimental setup (a);  $S_{21}$  phase of SAW in bare YX-128° cut LiNbO<sub>3</sub> substrate shifted with increased temperature (b) and corresponding linear dependence of a 120 MHz SAW phase shift as a function of temperature (c); SAW phase shift (left  $y$ -axis) and corresponding substrate temperature increase (right  $y$  axis) induced by 808 nm cw laser at a varied power density in samples with a monolayer of Au nanostars (Sample A) and coupled Au particles (Sample B) deposited on LiNbO<sub>3</sub> substrate. Corresponding values measured on bare LiNbO<sub>3</sub> substrate are shown with open squares (d).

However, the sample width is 1 cm. So, we probe the properties only in the central part of the sample, which is exposed with a laser beam 1 mm diameter. By changing the beam spot size, we experimentally found that beam size corresponds to the largest signal (SAW phase alteration). Note that with too tight focusing, the heat flow rate to unexposed areas increases as the temperature gradient increases. Thus, we have chosen the beam spot close to the SAW channel width. The examined sample is mounted and tightly pressed on the top of these two substrates near their edges in a “surface to surface” position so that a SAW generated by the first IDT may readily propagate via all three LiNbO<sub>3</sub> substrates and be detected by the second IDT. A SAW  $S_{21}$  phase shift and attenuation are measured with a network analyzer Obzor 103 as a function of sample temperature while direct heating or/and of a laser power when heating with light. A photothermal effect in nanoparticles induced by laser radiation and MIT in VO<sub>2</sub> film is accurately characterized in this manner. Previously, a simplified version of this setup was used by us to monitor the conductivity alteration in ZnO and Zn(Mg,Al)O films under deep UV/UV radiation exposure [25,26].

### 3. Results

#### 3.1. Setup Calibration Procedure

First, a temperature-induced phase shift of the SAW at 120 MHz, propagating in bare YX-128° cut LiNbO<sub>3</sub> substrate, was characterized. The temperature of the substrate was controlled in the range of 30–80 °C with an accuracy of ~0.1 °C by using a home-built Peltier heater. The SAW  $S_{21}$  phase shifts were measured at varied temperatures, as shown in Figure 2b. SAW attenuation is not altered when the LiNbO<sub>3</sub> crystal is heated, as its conductivity remains constant. This linear SAW phase shift versus temperature dependence shown in Figure 2c with the SAW phase shift of 20.7 induced by temperature change for every 1 °C is used in further experiments as a calibration plot to accurately monitor the temperature of the samples' surface in the further studies.

#### 3.2. SAW to Probe Photothermal Effect in Monolayers of Single Nanostars and Monolayer of Au Coupled Nanoparticles

One may monitor the average temperature of any nanoobjects or film deposited onto the LiNbO<sub>3</sub> crystal by using the calibration curve discussed above. Note that in the more general case, the temperature alteration may be induced by any physical or chemical phenomena. In particular, this allows us to characterize a photothermal effect induced in hybrid plasmonic systems when exposed to laser radiation.

Laser light at 808 nm was focused to a 1 mm round spot on the sample's surface in the central part where the SAW is propagating, as shown in Figure 2a. The light power density was controlled in the range of 2.7–27 W/cm<sup>2</sup> by using pulse width modulated electric triggering of the CW laser. The SAW phase shift and the corresponding temperature increase (obtained from the calibration curve) on the surface of Sample A with Au nanostars and Sample B with a monolayer of Au-coupled nanoparticle on bare LiNbO<sub>3</sub> substrate is shown in Figure 2d. The temperature increases by 3.7 °C and 5 °C in the case of samples A and B, correspondingly when exposed to 25 W/cm<sup>2</sup> laser light. Note that the temperature of a bare LiNbO<sub>3</sub> substrate is increased to only ~1.5 °C when similar light exposure is used, as shown with open rectangles in Figure 3d. The laser-induced heating of the bare substrate is occurred due to nonzero optical absorption in LiNbO<sub>3</sub> crystal. Optical transmission of LiNbO<sub>3</sub> crystal in the visible/near IR range is shown in Figure 1c.

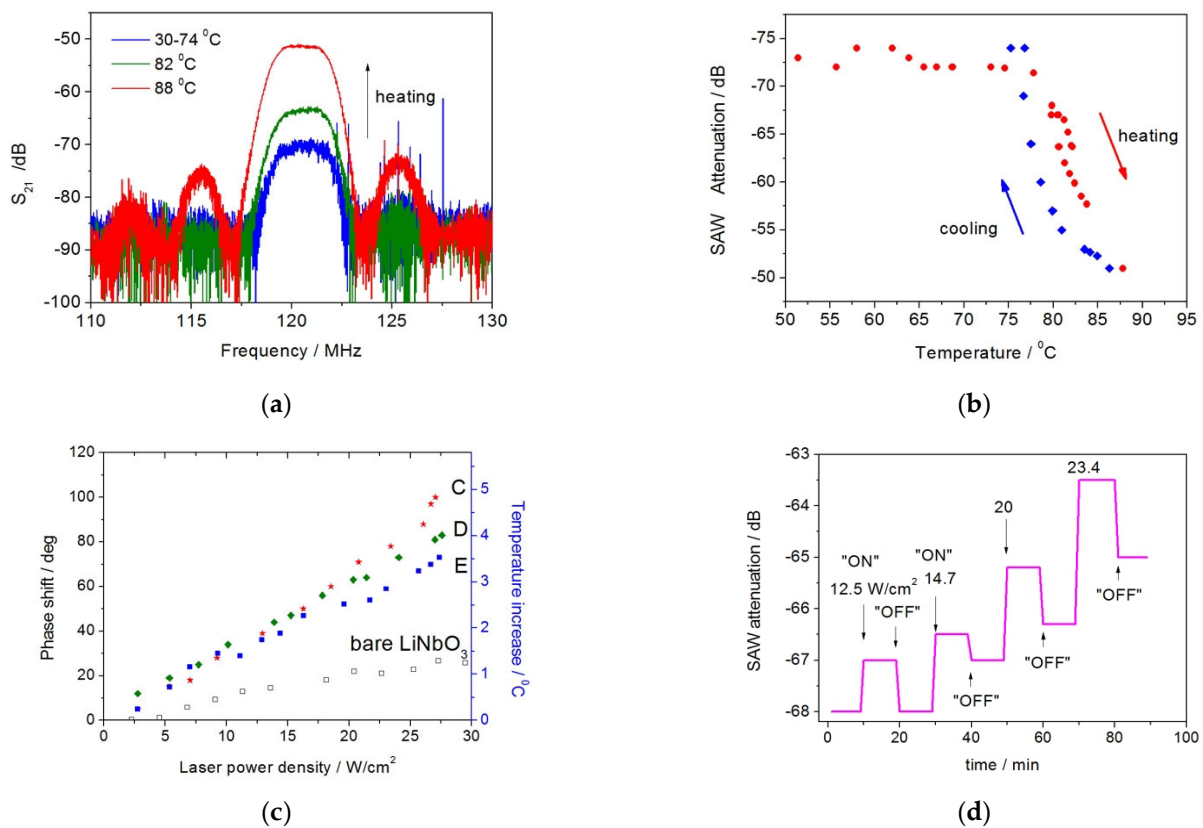


**Figure 3.**  $S_{21}$  characteristics of AuNSts/VO<sub>2</sub>/TiO<sub>2</sub> structure (Sample E) during MIT triggered by temperature (a); altered SAW attenuation in Sample E while temperature triggered MIT. Sample heating and cooling are shown with red and blue points respectively (b); SAW phase shift and corresponding surface temperature of Samples C–E and bare LiNbO<sub>3</sub> substrate when exposed with incident 808 nm laser light at different power density (c); SAW attenuation in Sample E measured at applied constant thermal heating up to 74 °C and additional 808 nm light exposure at varied (increased) power. "ON/OFF" corresponds to light switching on/off (d).

### 3.3. SAW to Probe the Temperature Induced MIT in "Au Nanostars/VO<sub>2</sub>" System

The temperature-induced metal-to-insulator transition in samples with AuNSts/VO<sub>2</sub>/TiO<sub>2</sub> structures deposited on the LiNbO<sub>3</sub> substrate with varied Au nanostars coverage (Samples C–E) was characterized by monitoring both the SAW attenuation and the phase shift as shown Figure 3.

When the insulator-to-metal transition in VO<sub>2</sub> film occurs at 74 °C, the SAW attenuation is decreased from 70 dB to 51 dB at 88 °C due to sheet resistance alteration, as shown in Figure 3a,b. Note that SAW attenuation in VO<sub>2</sub>/TiO<sub>2</sub>/LiNbO<sub>3</sub> sample is increased from 62 dB to 70 dB upon the deposition of Au nanostars. SAW attenuation in Sample E as a function of temperature for heating and cooling regimes is shown in Figure 3b. Both the SAW phase shifts and SAW attenuation were measured at varied temperatures simultaneously in Samples C–E. Upon complete thermal balancing, the sample surface temperature obtained from the SAW phase shift data revealed a great correlation with the value measured by the thermo-resistive sensor, which was mounted on the heater near the back side of the sample. However, when measuring both values immediately after increasing the heating power, i.e., before thermalization, the temperature on the surface revealed a somewhat lower value compared to one of the sensors and became equal upon some delay.

Next, Samples C–E were exposed to 808 nm laser light at varied power densities instead of direct heating. The obtained SAW phase shifts (right y axis), as well as the corresponding temperature (left y axis), are shown in Figure 3c. The photothermal effect,

i.e., the surface temperature increase due to light-induced light heating of Au nanostars, was characterized in this manner. Samples C–E temperature is increased up to 3.5 or 5 °C per different amounts of nanostars deposited on the surface, as shown in Figure 3c. Indeed, it is quite apparent that the samples with a larger amount of nanostars show a greater photothermal effect.

### 3.4. SAW to Probe the MIT Induced by Combination of Heating and Light Exposure

Finally, the combined switching of AuNSts/VO<sub>2</sub>/TiO<sub>2</sub> structures was studied. Sample E was heated to the temperature of 74 °C just at the beginning of MIT. Next, the sample was exposed to laser light at 808 nm with power density controlled between 12.5 and 23.4 W/cm<sup>2</sup>. The laser power was controlled by the PWM triggering of a cw laser. Laser “ON/OFF” cycles were chosen to be 10 min, enough for guaranteed stabilization of VO<sub>2</sub> temperature and conductivity. As the VO<sub>2</sub> film grown on TiO<sub>2</sub>/LiNbO<sub>3</sub> substrate has not abrupt but quite gradual MIT dynamics, one should increase the temperature to ~11 °C to completely switch the film to a metallic state (see Figure 3b). However, when exposed to light irradiance lower than ~23 W/cm<sup>2</sup>, the photothermal effect induced by plasmonic particles results in a temperature increase of ~3 °C or less. Therefore a complete switching of this VO<sub>2</sub> film at such applied laser power does not occur. Instead, the film may be switched to one of the metastable states defined by incident light irradiance, as shown in Figure 3d. Namely, once Sample E is exposed to 12.5 W/cm<sup>2</sup> light, the temperature is slightly increased in accordance with the corresponding curve in Figure 3c, and the SAW attenuation decreases from 68 dB to 67 dB claiming increased film conductivity. Upon switching off the additional heating light, VO<sub>2</sub> is returned to the initial conductivity state. If the sample is heated with larger light power, for instance, with 14.7 W/cm<sup>2</sup>, the SAW attenuation is decreased from 68 dB to 66.5 dB. Still, it does not return to 68 dB even after 10 min, claiming that film conductivity is increased and remains in some intermediate metastable state. A similar scenario with metastable states is observed for all cases when exposing VO<sub>2</sub> to light at higher power, as shown in Figure 3d.

The conductivity changes in VO<sub>2</sub> result in the altered SAW attenuation range of 68 dB and 63.5 dB. Therefore, the state of partially switched VO<sub>2</sub> film can be accurately controlled.

### 3.5. Composition and Lattice Vibrations of VO<sub>2</sub> Films on TiO<sub>2</sub>/LiNbO<sub>3</sub> Substrates

To better understand the origin of unusual metastable states in VO<sub>2</sub> films prepared on TiO<sub>2</sub>/XY-128° LiNbO<sub>3</sub> substrates, the samples were studied with X-ray photoelectron spectroscopy and Raman spectroscopy at altered temperature.

A typical XPS spectrum of VO<sub>2</sub>/TiO<sub>2</sub> film used in Samples C–E is shown in Figure 1e. XPS spectra reveal V 2p<sub>3/2</sub>, V 2p<sub>1/2</sub> and O 1s peaks. V 2p<sub>3/2</sub>, V 2p<sub>1/2</sub> mountains reveal a composition of V<sup>4+</sup> and V<sup>5+</sup> oxidation states. Namely, the more substantial peaks at 516.7 eV and 524.3 eV were assigned to be V 2p<sub>3/2</sub>, V 2p<sub>1/2</sub> of V<sup>5+</sup> oxidation state, and weaker peaks at 515.4 eV and 522.4 eV do correspond to V 2p<sub>3/2</sub> and V 2p<sub>1/2</sub> of V<sup>4+</sup> oxidation state [27,28]. The VO<sub>2</sub> phase in the V<sup>5+</sup> oxidation state is ~3.7 times greater than the VO<sub>2</sub> phase in the V<sup>4+</sup> state. The O 1s peak does also reveal two components. The less intense peak at 529.6 eV corresponds to oxygen bound to vanadium atoms in V<sup>4+</sup> and V<sup>5+</sup> oxidation states [27,28]. The stronger peak at 531.6 eV likely corresponds to oxygen [29] or/and OH groups [30,31] adsorbed on the surface. Some authors also assign this peak as a state corresponding to oxygen vacancies inside the film [31]. However, further efforts should be made to come to such a conclusion. The film is completely oxidized, and no traces of metallic vanadium are detected (not shown here).

Raman spectra of VO<sub>2</sub>/TiO<sub>2</sub> film on LiNbO<sub>3</sub> substrate at 30 °C shown in Figure 1f reveal Ag<sup>n</sup> vibration modes at 191 and 224 cm<sup>-1</sup> of a monocline (M1) VO<sub>2</sub> lattice and a mode near 264 cm<sup>-1</sup> which is assigned to monocline (M2) phase of VO<sub>2</sub> [10,32]. However, a mode at 264 cm<sup>-1</sup> is often erroneously assigned to the M1 phase [32,33]. However, phase M1 is disappeared from spectra already at 65–70 °C, while traces of M2 mode are still detected even at a higher temperature of 90 °C. In addition, two extra narrow modes near

405–409  $\text{cm}^{-1}$  and 420  $\text{cm}^{-1}$  (not identified yet) appear at a temperature of 85–90 °C when MIT occurred. Due to several very intense and broad vibration modes of monocrystalline  $\text{LiNbO}_3$  substrate, other  $\text{VO}_2$  and  $\text{TiO}_2$  lattice modes could not be detected.

## 4. Discussion

### 4.1. On SAW to Probe Photothermal Effect in Nanoparticles

The nonzero imaginary part of the dielectric function of gold results in great energy dissipation upon the light absorbed at wavelengths of nanoparticles plasmon in the near IR range. Photo-induced heating of a sample surface occurs. This corresponds to the first scenario of temperature increase. Besides, the electric field is tightly localized in the near field of a particle, typically no larger than ~10 nm from the particle surface. The electric field localization known as a “hot spot” is strongly dependent on the particle’s geometry and plasmonic coupling, if any. Suppose the medium which surrounds the particle is also capable of absorbing incident radiation. In that case, a “hot spot” may also induce extra heating, the second possible reason for the temperature increase.

In the studied samples with isolated or weakly coupled particles, the impact of the second plasmonic fields-related scenario seems much smaller compared to the first one, in which the light absorption in nanoparticles results in energy dissipation and further heat transfer to  $\text{VO}_2$ . Indeed, the comparison of the laser-induced surface temperature increase in Sample A in Figure 2d with AuNSTs and in Samples C–E with AuNSTs/ $\text{VO}_2$  in Figure 3c does not reveal a significant difference. As the AuNSTs in Samples A and C–E are contacting with  $\text{LiNbO}_3$  and  $\text{VO}_2$ , correspondingly, and the light absorption efficiency of these materials is different, the laser-induced heating of these surfaces should also be different if the plasmonic field effect would be strong. However, it is not the case here, evidencing that the plasmonic field effect is minor.

Despite the evidence that the plasmonic field-induced absorption mechanism in  $\text{VO}_2$  is minor in discussed samples, it does not mean it could not be significant in other plasmonic systems. We expect that in strongly coupled plasmonic systems, the impact of the “hot spots” related temperature increase channel could be much more pronounced. Also, it is notable that in  $\text{VO}_2$  with abrupt MIT, the thermal or plasmonic non-thermal effects, if any, do show a much more dramatic effect compared to those systems where  $\text{VO}_2$  has a slowly evolving transition and minor temperature increase induced by these effects is not able to trigger a complete transition. Besides, in typical  $\text{VO}_2/\text{c-Al}_2\text{O}_3$  films, the MIT evolves dramatically to the final metallic state once it has been triggered, which often makes it challenging to follow the process, especially if the temperature of the sample surface is not accurately monitored in situ.

Let’s briefly compare the main features of the proposed SAW-based method with several popular methods to study the temperature of individual nanoobjects or the entire surface. Luminescence nanothermometry typically reveals small spectral shifts of a broad luminescence spectrum of quantum dots for only 0.065 nm per °C, which defines quite a low accuracy which is not enough for characterizing small temperature alterations [34]. However, when monitoring a temperature-induced luminescence quenching rate change which for some QDs may approach 1% per °C, one may obtain a moderate temperature resolution between 0.2 and 1 °C [18]. The more accurate measurements with 0.1 °C achieved uncertainty are still quite rare for this approach [35]. Also, special corrections related to light-induced self-heating of nanothermometers should be taken into account to avoid errors. Besides, the measurement range should not exceed the temperature of QDs degradation, which is often not too high. Raman thermometry based on measuring of intensity, width or shifts of Stokes and anti-Stokes Raman modes does typically show shifts for 0.027  $\text{cm}^{-1}$  per °C [20], which are also too small to resolve the temperature alterations of 0.1 °C as a typical Raman spectrometer has a spectral resolution of 1  $\text{cm}^{-1}$  or worse. However, the method allows one to monitor very high temperatures, typically up to 700 °C, which makes it effective when studying nanosystems for thermoplasmonics [20]. The photothermal imaging method is based on monitoring local alterations of the refraction

index near nanoobjects heated by laser light [23]. Providing sub-diffraction resolution, the method best suits studying photothermal characteristics of single absorbing species at the nanoscale but not temperature distribution at large surfaces. Holographic interferometry is best suited for studying thick and transparent samples with large thermal expansion coefficients where the refractive index is significantly altered with temperature [22,36]. Note that thermo-optic coefficients of materials may be different for several orders of magnitude. For instance, the coefficients  $dn/dT$  for the fused silica and PMMA are roughly equal to  $8.46 \times 10^{-6} \text{ }^\circ\text{C}^{-1}$  and  $1.1 \times 10^{-4} \text{ }^\circ\text{C}^{-1}$ , correspondingly [36]. If the temperature-sensitive substrate material is properly chosen, one may obtain a high-temperature resolution of  $\pm 0.1 \text{ }^\circ\text{C}$  [21] or even as high as  $\pm 0.0085 \text{ }^\circ\text{C}$  [36].

The photothermal effect in Samples A and B with plasmonic particles is several times greater than in a bare  $\text{LiNbO}_3$  substrate which allows us to clearly distinguish the photo-induced heating effect exclusively associated with the plasmonic system (see Figure 2d). It should be emphasized that the  $\text{LiNbO}_3$  temperature alteration for only  $5 \text{ }^\circ\text{C}$  corresponds to a great SAW phase shift for  $\sim 100$  degrees. Taking into account electronic noise, we estimate the temperature measurement precision of our SAW-based technique to be not worse than  $0.2 \text{ }^\circ\text{C}$  with an uncertainty of  $\sim 0.1 \text{ }^\circ\text{C}$  when using wave at 120 MHz. It should be emphasized that if using SAW at a higher frequency, one would achieve even higher temperature resolution. Summarizing the above discussion, it should be claimed that the proposed SAW-based method is comparable or even better in temperature resolution and reliability compared with the best existing techniques, including optical interferometry [22], fluorescence nanothermometry [18] and Raman thermometry [20]. However, it is much more cost-effective and much less labor-consuming. More accurate direct comparison of the possibilities of proposed SAW based on optical interferometry and fluorescence nanothermometry as the most suitable alternatives is a subject for further study.

#### 4.2. On SAW to Probe Metal to Insulator Transition $\text{VO}_2$

The SAW velocity change ( $\Delta v$ ) and wave intensity attenuation ( $\Gamma$ ) are induced by acoustoelectric interaction with a film which is given by [37]:

$$\frac{\Delta v}{v_0} = \frac{k_{ef}^2}{2} \frac{1}{1 + \sigma_{sh}^2 / \sigma_M^2} \quad (1)$$

$$\Gamma = k_{ef}^2 \left( \frac{2\pi}{\lambda} \right) \frac{\sigma_{sh} / \sigma_M}{1 + \sigma_{sh}^2 / \sigma_M^2} \quad (2)$$

where  $v_0$ ,  $\lambda$ ,  $\sigma_{sh}$ ,  $k_{ef}^2 \approx 0.056$  and  $\sigma_M = v_0(\epsilon_s + \epsilon_0) = 1.48 \times 10^{-6} (\Omega/\square)^{-1}$  denote a SAW initial velocity in  $\text{LiNbO}_3$  (3880 m/s), wavelength, sheet conductivity of  $\text{VO}_2$  layer, effective electromechanical coupling coefficient and the material constant called Maxwell conductivity, respectively. Dielectric permittivity of  $\text{LiNbO}_3$  substrate  $\epsilon_s = 3.7 \times 10^{-10} \text{ F}\cdot\text{m}^{-1}$ . When the sheet conductivity of the  $\text{VO}_2$  film is limited to Maxwell conductivity  $\sigma_M$ , the attenuation  $\Gamma$  of a SAW approaches a maximum.

Indeed, the initial sheet conductivity  $\sigma_{sh}$  of the prepared  $\text{VO}_2$  film at room temperature may be smaller or greater than Maxwell conductivity  $\sigma_M$ . When the initial film conductivity  $\sigma_{sh}$  is greater than  $\sigma_M$  and is increased due to the MIT in  $\text{VO}_2$  film, the attenuation  $\Gamma$  is decreased. However, if the initial conductivity of a  $\text{VO}_2$  film prepared in some special conditions is smaller than  $\sigma_M$ , the attenuation could grow with increased conductivity. More information about similar phenomena may be found in our previous reports on SAW propagating in  $\text{Zn}(\text{Mg}, \text{Al})\text{O}$  and  $\text{ZnO}$  films [25,26].

Also, the SAW velocity and, thus, the measured phase of arriving SAW are significantly dependent on surface temperature, and the dependence of a SAW phase on  $\text{VO}_2$  sheet conductivity is minor.

#### 4.3. The Differences of MIT in VO<sub>2</sub>/Al<sub>2</sub>O<sub>3</sub> and VO<sub>2</sub>/TiO<sub>2</sub>/LiNbO<sub>3</sub> Films

Remarkably, the VO<sub>2</sub>/TiO<sub>2</sub> films grown on LiNbO<sub>3</sub> with gradual switching and intermediate metastable states along the MIT curve at which one may stabilize film conductivity are very different from traditional VO<sub>2</sub> films grown on the Al<sub>2</sub>O<sub>3</sub> substrates which we studied before [10]. Indeed, traditional VO<sub>2</sub>/Al<sub>2</sub>O<sub>3</sub> films typically show abrupt MIT once the process is triggered. Moreover, one can't stabilize the conductivity at any state within the isolator to the metal transition curve. Also, we do typically observe MIT in VO<sub>2</sub>/Al<sub>2</sub>O<sub>3</sub> films when the film is pre-heated by current to the beginning of the transition and additionally exposed with light at an irradiance of 0.4 W/cm<sup>2</sup> to 0.28 W/cm<sup>2</sup> (at 4 mm laser spot) [10] which is at least ~100 times lower compared to those needed for complete switching of VO<sub>2</sub>/TiO<sub>2</sub>/LiNbO<sub>3</sub>. The difference between irradiances can be explained by gradual MIT dynamics (~11 °C per transition) and larger heat flow at smaller laser spots.

In our previous Raman study of VO<sub>2</sub>/Al<sub>2</sub>O<sub>3</sub> films [10], we already reported on a mixture of M1 and M2 monocline lattices and their similar temperature behavior when the M1 phase disappeared after MIT at ~67 °C, and the M2 phase was not affected by temperature change [10].

Note that the VO<sub>2</sub>/TiO<sub>2</sub>/LiNbO<sub>3</sub> films in the present study show MIT at 74 °C, which is higher than in VO<sub>2</sub>/Al<sub>2</sub>O<sub>3</sub> films at 67 °C [10]. Indeed, the observed shifts of Ag<sub>n</sub> vibrations indicate the presence of mechanical stresses in the VO<sub>2</sub> lattice. The correlation of MIT shift and mechanical stresses in VO<sub>2</sub>/TiO<sub>2</sub> films was reported by several authors. However, a related MIT is typically shifted to a lower temperature [38,39]. Therefore, YX-128° cut LiNbO<sub>3</sub> substrate likely results in mechanically induced MIT shift to a higher temperature.

XPS study reveals a mixture of phases with a ratio of V<sub>2</sub>O<sub>5</sub>:VO<sub>2</sub> = 3.7 and likely existing oxygen vacancies in the VO<sub>2</sub> film, which is very different from the typical VO<sub>2</sub> films prepared [32,40] where the VO<sub>2</sub> phase is prevailing. Remarkable that a similar phase ratio transformation towards a greater V<sub>2</sub>O<sub>5</sub> amount was reported for films initially prepared at 500 °C by the e-beam evaporation method, which was further thermally oxidized at temperatures of 400–550 °C [33]. Note that the V<sub>2</sub>O<sub>5</sub> phase has an MIT at 280° [41] and can hardly be related to MIT at 74 °C or the memory effect observed in samples. However, a large V<sub>2</sub>O<sub>5</sub> phase and XPS peak at 531.6 eV, possibly related to oxygen vacancies in bulk or on the film surface, claims that some other oxygen-related reactions during the film design have occurred. We believe these formed oxygen-related features are responsible for the unusual memory effect in VO<sub>2</sub>/TiO<sub>2</sub> films. A detailed study of this phenomenon is to be continued. We believe that the proposed new type of VO<sub>2</sub> film grown on TiO<sub>2</sub>/LiNbO<sub>3</sub> with gradual MIT and memory effect in metastable conductivity states may be used in metasurfaces where gradient characteristics are desired, but slow tuning is not an issue.

## 5. Conclusions

In conclusion, we propose a new method based on surface acoustic waves to accurately monitor a photothermal effect in plasmonic nanosystems and plasmon-enhanced MIT in VO<sub>2</sub>-based composites. Measuring a 120 MHz SAW phase shift in temperature-unstable LiNbO<sub>3</sub> substrate, we acquire the surface temperature data with a resolution of ±0.1 °C. Simultaneously, by probing the SAW attenuation, one may monitor the conductivity change during the MIT in VO<sub>2</sub>. A monolayer of isolated Au nanostars and coupled Au nanoparticles boost the photothermal effect, which increases the VO<sub>2</sub> surface temperature by 5 °C and 3.7 °C, respectively, when exposing the sample to laser light at 25 W/cm<sup>2</sup>.

The VO<sub>2</sub>/TiO<sub>2</sub>/LiNbO<sub>3</sub> films reveal an option to stabilize their conductivity at any point within the MIT curve and accurately tune it by increasing incident light power which is very different from the behavior of similar films prepared on Al<sub>2</sub>O<sub>3</sub> or TiO<sub>2</sub> substrates. We believe that this unique memory effect of the prepared structures will be demanding for designing tunable middle IR/THz optical devices, namely mirrors with controlled reflection, frequency filters, metalens with tunable focus, gradient gratings and others. Furthermore, in a broader scale, the proposed SAW-based method may be placed in one row with the best available optical methods for temperature monitoring, including

optical interferometry, fluorescence nanothermometry and Raman thermometry. It will be useful for characterizing the photothermal effect in hybrid nanosystems, metasurfaces and optoelectronic devices.

**Author Contributions:** Conceptualization, V.K.; SAW measurements, V.K.; nanostars synthesis and deposition, B.K.; coupled particles deposition, V.K.; VO<sub>2</sub>/TiO<sub>2</sub> films deposition, M.K. and E.K.; writing—original draft preparation, V.K. and B.K.; XPS measurements and analysis, A.N. and A.K. (Alexey Kozakov); Raman measurements and analysis, A.K. (Alexey Konstantinov), V.K. and A.M.; review and editing, E.K. and G.K.; supervision, E.K. All authors have read and agreed to the published version of the manuscript.

**Funding:** The SAW-based characterization of photothermal effects was funded by Russian Science Foundation, grant № 22-29-01037 at SFU. The deposition, optimization of VO<sub>2</sub>/TiO<sub>2</sub> films, XPS and Raman measurements were funded by the Ministry of Science and Higher Education of the Russian Federation (State assignment in scientific activity № FENW-2023-0014). The preparation and characterization of Au nanostars were funded by Russian Science Foundation, grant № 23-24-00062.

**Institutional Review Board Statement:** Not applicable.

**Informed Consent Statement:** Not applicable.

**Data Availability Statement:** Not applicable.

**Conflicts of Interest:** The authors declare no conflict of interest.

## References

1. Cuffe, S.; John, J.; Zhang, Z.; Parra, J.; Sun, J.; Orobtschouk, R.; Ramanathan, S.; Sanchis, P. VO<sub>2</sub> nanophotonics. *APL Photonics* **2020**, *5*, 110901. [[CrossRef](#)]
2. He, J.; Dong, T.; Chi, B.; Zhang, Y. Metasurfaces for terahertz wavefront modulation: A review. *J. Infrared Millim. Terahertz Waves* **2020**, *41*, 607–631. [[CrossRef](#)]
3. Zhang, X.; Tian, Z.; Yue, W.; Gu, J.; Zhang, S.; Han, J.; Zhang, W. Broadband Terahertz Wave Deflection Based on C-shape Complex Metamaterials with Phase Discontinuities. *Adv. Mater.* **2013**, *25*, 4567–4572. [[CrossRef](#)] [[PubMed](#)]
4. Wang, T.; He, J.; Guo, J.; Wang, X.; Feng, S.; Kuhl, F.; Becker, M.; Polity, A.; Klar, P.J.; Zhang, Y. Thermally switchable terahertz wavefront metasurface modulators based on the insulator-to-metal transition of vanadium dioxide. *Opt. Express* **2019**, *27*, 20347–20357. [[CrossRef](#)] [[PubMed](#)]
5. Liu, L.; Zhang, X.; Kenney, M.; Su, X.; Xu, N.; Ouyang, C.; Shi, Y.; Han, J.; Zhang, W.; Zhang, S. Broadband Metasurfaces with Simultaneous Control of Phase and Amplitude. *Adv. Mater.* **2014**, *26*, 5031–5036. [[CrossRef](#)] [[PubMed](#)]
6. Driscoll, T.; Kim, H.T.; Chae, B.G.; Kim, B.J.; Lee, Y.W.; Jokerst, N.M.; Palit, S.; Smith, D.R.; Ventra, M.D.; Basov, D.N. Memory metamaterials. *Science* **2009**, *325*, 1518–1521. [[CrossRef](#)]
7. Cai, H.; Chen, S.; Zou, C.; Huang, Q.; Liu, Y.; Hu, X.; Fu, Z.; Zhao, Y.; He, H.; Lu, Y. Multifunctional Hybrid Metasurfaces for Dynamic Tuning of Terahertz Waves. *Adv. Opt. Mater.* **2018**, *6*, 1800257. [[CrossRef](#)]
8. Pan, M.; Fu, Y.; Zheng, M.; Chen, H.; Zang, Y.; Duan, H.; Li, Q.; Qiu, M.; Hu, Y. Dielectric metalens for miniaturized imaging systems: Progress and challenges. *Light Sci. Appl.* **2022**, *11*, 195. [[CrossRef](#)]
9. Tian, H.W.; Shen, H.Y.; Zhang, X.G.; Li, X.; Jiang, W.X.; Cui, T.J. Terahertz Metasurfaces: Toward Multifunctional and Programmable Wave Manipulation. *Front. Phys.* **2020**, *8*, 584077. [[CrossRef](#)]
10. Kaydashev, V.E.; Slavich, A.S.; Domaratskiy, I.K.; Zhukov, S.S.; Kirtaev, R.; Mylnikov, D.A.; Kutepov, M.E.; Kaidashev, E.M. Electrically reduced optical switching threshold of VO<sub>2</sub>-based THz metasurface. *arXiv* **2022**, arXiv:2204.13427.
11. Baffou, G.; Polleux, J.; Rigneault, H.; Monneret, S. Super-Heating and Micro-bubble Generation around Plasmonic Nanoparticles under cw illumination. *J. Phys. Chem. C* **2014**, *118*, 4890–4898. [[CrossRef](#)]
12. Baffou, G.; Quidant, R.; Girard, C. Heat generation in plasmonic nanostructures: Influence of morphology. *Appl. Phys. Lett.* **2009**, *94*, 153109. [[CrossRef](#)]
13. Govorov, A.O.; Richardson, H.H. Generating heat with metal nanoparticles. *Nanotoday* **2007**, *2*, 30–38. [[CrossRef](#)]
14. Metwally, K.; Mensah, S.; Baffou, G. Isosbestic Thermoplasmonic Nanostructures. *ACS Photonics* **2017**, *4*, 1544–1551. [[CrossRef](#)]
15. Galanzha, E.I.; Nedosekin, D.A.; Sarimollaoglu, M.; Orza, A.I.; Biris, A.S.; Verkhusha, V.V.; Zharov, V.P. Photoacoustic and photothermal cytometry using photoswitchable proteins and nanoparticles with ultrasharp resonances. *J. Biophotonics* **2015**, *8*, 687. [[CrossRef](#)] [[PubMed](#)]
16. Cui, Y.; He, Y.; Jin, Y.; Ding, F.; Yang, L.; Ye, Y.; Zhong, S.; Li, Y.; He, S. Plasmonic and metamaterial structures as electromagnetic absorbers. *Laser Photonics Rev.* **2014**, *8*, 495–520. [[CrossRef](#)]
17. Molesky, S.S.; Dewalt, C.J.; Jacob, Z. High Temperature Epsilon-Near-Zero and Epsilon-Near-Pole Metamaterial Emitters for Thermophotovoltaics. *Opt. Express* **2013**, *21*, A96–A110. [[CrossRef](#)]
18. Jaque, D.; Vetrone, F. Luminescence nanothermometry. *Nanoscale* **2012**, *4*, 4301. [[CrossRef](#)]

19. Coppens, Z.J.; Li, W.; Walker, D.G.; Valentine, J.G. Probing and Controlling Photothermal Heat Generation in Plasmonic Nanostructures. *Nano Lett.* **2013**, *13*, 1023–1028. [[CrossRef](#)]
20. Kharintsev, S.S.; Chernykh, E.A.; Shelaev, A.V.; Kazarian, S.G. Nanoscale Sensing Vitrification of 3D Confined Glassy Polymers Through Refractory Thermoplasmonics. *ACS Photonics* **2021**, *8*, 1477–1488. [[CrossRef](#)]
21. Wang, Q.; Zhao, J.; Jiao, X.; Di, J.; Jiang, H. Visual and quantitative measurement of the temperature distribution of heat conduction process in glass based on digital holographic interferometry. *J. Appl. Phys.* **2012**, *111*, 093111. [[CrossRef](#)]
22. Belashov, A.V.; Petrov, N.V.; Semenova, I.V. Accuracy of image-plane holographic tomography with filtered backprojection: Random and systematic errors. *Appl. Opt.* **2016**, *55*, 81–88. [[CrossRef](#)] [[PubMed](#)]
23. Boyer, D.; Tamarat, P.; Maali, A.; Lounis, B.; Orrit, M. Photothermal Imaging of Nanometer-Sized Metal Particles Among Scatterers. *Science* **2002**, *297*, 1160–1163. [[CrossRef](#)] [[PubMed](#)]
24. Pazos-Perez, N.; Guerrini, L.; Alvarez-Puebla, R.A. Plasmon Tunability of Gold Nanostars at the Tip Apexes. *ACS Omega* **2018**, *3*, 17173–17179. [[CrossRef](#)] [[PubMed](#)]
25. Kutepov, M.E.; Kaydashev, V.E.; Karapetyan, G.Y.; Minasyan, T.A.; Chernyshev, A.V.; Abdulkhaidov, K.G.; Shevtsova, S.I.; Glazunova, E.V.; Irkha, V.A.; Kaidashev, E.M. Deep UV light sensitive Zn<sub>1-x</sub>YMg<sub>x</sub>Al<sub>y</sub>O films with fast photoelectric response for SAW photodetectors. *Smart Mater. Struct.* **2019**, *28*, 065024. [[CrossRef](#)]
26. Karapetyan, G.Y.; Kaydashev, V.E.; Zhilin, D.A.; Minasyan, T.A.; Abdulkhaidov, K.G.; Kaidashev, E.M. Use of multiple acoustic reflections to enhance SAW UV photo-detector sensitivity. *Smart Mater. Struct.* **2017**, *26*, 035029. [[CrossRef](#)]
27. Sawatzky, G.A.; Antonides, E. The electronic structure and electron correlation effects studied by XPS. *J. Phys. Colloq.* **1976**, *37*, 4–117. [[CrossRef](#)]
28. Demeter, M.; Neumann, M.; Reichelt, W. Mixed-valence vanadium oxides studied by XPS. *Surf. Sci.* **2000**, *41*, 454–456. [[CrossRef](#)]
29. Kozakov, A.T.; Kochur, A.G.; Reznichenko, L.A.; Shilkina, L.A.; Pavlenko, A.V.; Nikolskii, A.V.; Googlev, K.A.; Smotrakov, V.G. Single-crystal rare earths manganites La<sub>1-x-y</sub>Bi<sub>x</sub>A<sub>y</sub>Mn<sub>α</sub>O<sub>3±β</sub> (A = Ba, Pb): Crystal structure, composition, and Mn ions valence state. X-ray diffraction and XPS study. *J. Electron Spectrosc. Relat. Phenom.* **2013**, *186*, 14–24. [[CrossRef](#)]
30. Kozakov, A.T.; Kochur, A.G.; Nikolskii, A.V.; Raevski, I.P.; Kubrin, S.P.; Raevskaya, S.I.; Titov, V.V.; Gusev, A.A.; Isupov, V.P.; Li, G.; et al. Valence state of B and Ta cations in the AB<sub>1/2</sub>Ta<sub>1/2</sub>O<sub>3</sub> ceramics (A = Ca, Sr, Ba, Pb; B = Fe, Sc) from X-ray photoelectron and Mossbauer spectroscopy data. *J. Electron Spectrosc. Relat. Phenom.* **2020**, *239*, 146918. [[CrossRef](#)]
31. Banger, K.K.; Yamashita, Y.; Mori, K.; Peterson, R.L.; Leedham, T.; Rickard, J.; Siringhaus, H. Low-temperature, high-performance solution-processed metal oxide thin-film transistors formed by a “sol–gel on chip” process. *Nat. Mater.* **2010**, *10*, 45–50. [[CrossRef](#)]
32. Zhou, X.; Zhao, L.; Zhen, W.; Lin, Y.; Wang, C.; Pan, T.; Li, L.; Du, G.; Lu, L.; Cao, X.; et al. Phase-Transition-Induced VO<sub>2</sub> Thin Film IR Photodetector and Threshold Switching Selector for Optical Neural Network Applications. *Adv. Electron. Mater.* **2021**, *7*, 2001254. [[CrossRef](#)]
33. Ureña-Begara, F.; Crunteanu, A.; Raskin, J. Raman and XPS characterization of vanadium oxide thin films with temperature. *Appl. Surf. Sci.* **2017**, *403*, 717–727. [[CrossRef](#)]
34. Skaptsova, A.A.; Gofmana, V.V.; Galushka, V.V.; Markin, A.V.; Kochubey, V.I.; Goryacheva, I.Y. Thermosensitivity of Nanothermometer: CdSe/ZnS vs. CuInS<sub>2</sub>/ZnS. In Proceedings of the Saratov Fall Meeting 2015: Third International Symposium on Optics and Biophotonics and Seventh Finnish-Russian Photonics and Laser Symposium (PALS), Saratov, Russia, 21 April 2016; Volume 9917, p. 991712.
35. Baffou, G.; Kreuzer, M.P.; Kulzer, F.; Quidant, R. Temperature mapping near plasmonic nanostructures using fluorescence polarization anisotropy. *Opt. Express* **2009**, *17*, 3291–3298. [[CrossRef](#)] [[PubMed](#)]
36. Ito, A.; Kashiwagi, T. Measurement technique for determining the temperature distribution in a transparent solid using holographic interferometry. *Appl. Opt.* **1987**, *26*, 954–958. [[CrossRef](#)]
37. Wixforth, A.; Scriba, J.; Wassermeier, M.; Kotthaus, J.P.; Weimann, G.; Schlapp, W. Surface acoustic waves on GaAs/AlxGa<sub>1-x</sub>As heterostructures. *Phys. Rev. B* **1989**, *40*, 7874–7887. [[CrossRef](#)]
38. Chen, B.; Kim, G.; Cho, H.J.; Ohta, H. Room Temperature Insulator-to-Metal Transition of VO<sub>2</sub>/TiO<sub>2</sub> Epitaxial Bilayer Films Grown on M-plane Sapphire Substrates. *Adv. Electron. Mater.* **2022**, *8*, 2100687. [[CrossRef](#)]
39. Muraoka, Y.; Hiroi, Z. Metal–insulator transition of VO<sub>2</sub> thin films grown on TiO<sub>2</sub> (001) and (110) substrates. *Appl. Phys. Lett.* **2002**, *80*, 583–585. [[CrossRef](#)]
40. Ding, Z.; Cui, Y.; Wan, D.; Luo, H.; Gao, Y. High-performance thermal sensitive VO<sub>2</sub>(B) thin films prepared by sputtering with TiO<sub>2</sub>(A) buffer layer and first-principles calculations study. *RSC Adv.* **2017**, *7*, 29496–29504. [[CrossRef](#)]
41. Kang, M.; Kim, I.; Kim, S.W.; Ryu, J.W.; Yeol, H. Metal-insulator transition without structural phase transition in V<sub>2</sub>O<sub>5</sub> film. *Appl. Phys. Lett.* **2011**, *98*, 131907. [[CrossRef](#)]

**Disclaimer/Publisher’s Note:** The statements, opinions and data contained in all publications are solely those of the individual author(s) and contributor(s) and not of MDPI and/or the editor(s). MDPI and/or the editor(s) disclaim responsibility for any injury to people or property resulting from any ideas, methods, instructions or products referred to in the content.